DOI: 10.19884/j.1672-5220.202405004

Design and Synthesis of Molybdenum Red Cluster $\{Mo_{49}\}$ by Building Block-Directed Assembly for Proton Conduction

ZHANG Duidui[1], CHEN Zeyu[1], TANG Rongqing[1], GONG Tengfei[2], SHAO Zhiyu[1*], XUAN Weimin[1*]
1. State Key Laboratory of Advanced Fiber Materials, College of Chemistry and Chemical Engineering, Donghua University, Shanghai 201620, China
2. Jiaxing Jiayuan Inspection Technology Service Co., Ltd., Jiaxing 314000, China

Abstract: Highly reduced molybdenum red (MR) clusters have emerged as a new type of polyoxomolybdates (POMos) and showed great potential as electron/proton reservoirs for energy conversion and storage, as well as for catalysis. However, the limited structural diversity of MR clusters significantly hinders further exploration of their potential as functional materials. Herein, we describe the synthesis of a novel highly reduced MR cluster $\{Mo_{49}\}$ (compound 1) based on rational assembly of a variety of basic building blocks (BBs). In addition to the well-established BBs found in the family of MR clusters, the unique tetrahedral $\{Mo^{VI}_4\}$ BB plays a key role in directing the assembly to afford trigonal pyramid-like structure of compound 1. The POMo scaffold consists of 49 Mo and 148 O atoms and exhibits a high reduction degree of 73%. Moreover, at 80 ℃ and 98% relative humidity (RH), the pellet sample of compound 1 displays a high proton conductivity of 7.88×10^{-3} S/cm owing to the efficient hydrogen-bonded network built from the surface oxygen atoms, protons and guest water molecules. This research offers new insights into the assembly and synthesis of MR clusters through a BB strategy and manifests their significant potential for advanced applications.

Keywords: polyoxomolybdate (POMo); highly reduced cluster; building block (BB); proton conductivity
CLC number: O641 **Document code**: A
Article ID: 1672-5220(2025)03-0230-12

Open Science Identity (OSID)

0 Introduction

Polyoxometalates (POMs) are a class of discrete anionic inorganic clusters built up by early transition metal-oxo units and show diverse applications in the fields of chemistry and materials[1-5]. With the inherent reversible redox property, POMs can easily transform into reduced clusters via chemical, photochemical and electrochemical reduction[6-12]. These electron-rich species are excellent electron reservoirs for catalysis, biomedicine and energy-based applications[13-21]. Meanwhile, the highly negative charge endowed by reduced electrons facilitates the attraction of protons as counterion, which in turn reinforces the proton conduction performance[22-25]. As such, the completely reduced hourglass-type $M\{P_4Mo_6\}_2$ and highly reduced $\{Mo_{240}\}$ exhibit high proton conduction performance[26-29].

Owing to the facile redox potential of the Mo^{VI}/Mo^{V} couple, polyoxomolybdates (POMos) constitute a majority of reduced POM clusters, including archetypal molybdenum blue and molybdenum brown clusters such as $\{Mo_{368}\}$[30], $\{Mo_{176}\}$[31], $\{Mo_{154}\}$[32] and $\{Mo_{132}\}$[33]. As an emerging type of reduced clusters, molybdenum red (MR) clusters feature a high reduction degree which is in general more than 50%. Based on the ordered assembly of basic building blocks (BBs), the family of MR clusters has greatly expanded from $\{Mo_{12}\}$ to high-nuclearity $\{Mo_{240}\}$[34-35]. Despite these notable developments, MR clusters still suffer from limited structural variety compared with well-established molybdenum blue and molybdenum brown counterparts, which dramatically impedes further exploration of such clusters as functional materials. To extend the structural library of MR clusters, the key point is to generate new BBs that can direct the assembly of novel structures[36-43]. Our recent work showed that the in situ formed $\{Mo^{V}_4\}$ BB was viable to induce the aggregation of a variety of MR clusters ranging from $\{Mo_{28}\}$ to $\{Mo_{40}\}$, further confirming the significance of the BB strategy[44].

Herein we demonstrate the design and synthesis of a trigonal pyramid-like MR cluster $\{Mo_{49}\}$ (compound 1) for proton conduction. Compound 1 consists of five types of different Mo—O BBs. During the assembly, the

Received date: 2024-05-15
Foundation items: National Natural Science Foundation of China (Nos. 92161111 and 21901038); Program for Professor of Special Appointment (Eastern Scholar) at Shanghai Institutions of Higher Learning, China; International Cooperation Fund of Science and Technology Commission of Shanghai Municipality, China (No. 21130750100)
* Correspondence should be addressed to SHAO Zhiyu, email: zyshao@dhu.edu.cn; XUAN Weimin, email: weiminxuan@dhu.edu.cn
Citation: ZHANG D D, CHEN Z Y, TANG R Q, et al. Design and synthesis of molybdenum red cluster $\{Mo_{49}\}$ by building block-directed assembly for proton conduction [J]. *Journal of Donghua University (English Edition)*, 2025, 42(3): 230-241.

classical {Mo^{V}_{2}}, cyclic {Mo^{V}_{6}} and tripodal {Mo^{V}_{6}} BBs first aggregate into a tetrahedral skeleton {Mo^{V}_{36}}, which is further capped by three {Mo^{VI}_{3}} BBs and one novel {Mo^{VI}_{4}} BB on the base to afford {Mo_{49}}, with a reduction degree up to 73%. Due to the presence of an extensive proton-hopping pathway derived from oxygen-rich {Mo_{49}}, proton counterions and guest water molecules, compound 1 displays good proton conductivity of 7.88×10^{-3} S/cm. Compound 1 is characterized crystallographically and its formula is confirmed by a variety of analytical techniques as $K_{15}H_5[Mo^{V}_{36}Mo^{VI}_{13}(OH)_{18}O_{130}] \cdot 58\ H_2O$.

1 Experimental Section

1.1 Materials and methods

K_2MoO_4 and CH_3COOK were purchased from Titan Scientific Co., Ltd., Shanghai, China. $N_2H_4 \cdot 2HCl$ was purchased from Bidepharm Co., Ltd., Shanghai, China. Other chemicals were purchased from Sinopharm Chemical Reagent Co., Ltd., Shanghai, China. All commercially available reagents were analytically pure and used as received without further purification.

The Fourier transform infrared (FTIR) spectroscopy was performed on a Nicolet iS50 FTIR spectrometer (Thermo Fisher, USA) in a range of 500–4 000 cm^{-1}. The powder X-ray diffraction (XRD) pattern was collected on a D8 ADVANCE instrument (Bruker, Germany) with Cu Kα radiation in a 2θ range of 3° to 50° at a scanning rate of 0.02 (°)/s. Thermogravimetric analysis (TGA) was performed on a TG8000 thermogravimetric analyzer (Mettler Toledo, Switzerland), under nitrogen flow at a typical heating rate of 10 ℃/min from 30 to 800 ℃. The H atom mass fraction was determined by a VARIO EL III elemental analyzer (Elementar Analysensysteme GmbH, Germany). Elemental mass fractions of Mo and K were determined by inductivity-coupled plasma optical emission spectroscopy (ICP-OES) using a Teledyne Leeman Prodigy Plus spectrometer (Teledyne Leeman Labs, USA). The Raman spectra were acquired with a Renishaw inVia Reflex laser Raman spectrometer (Renishaw plc, UK).

1.2 Synthesis of compound 1

K_2MoO_4 (1.98 mmol), $N_2H_4 \cdot 2HCl$ (0.62 mmol) and CH_3COOK (0.50 mmol) were dissolved in deionized water (6 mL) and the mixture was stirred for 30 min. After that, the pH value of the reaction system was adjusted to around 4.7 by adding 6 mol/L HCl solution and stirring for about 45 min until the solution color was deep green. Subsequently, the Mo-containing aqueous solution was transferred to a 10 mL Teflon-lined stainless-steel container, kept at 120 ℃ for 72 h, and then slowly cooled to room temperature. The deep red crystals were collected and washed with ethanol (yield of 18% based on Mo). Elemental mass fractions calculated (found): H 1.61% (1.59%), K 6.72% (6.93%), Mo 53.89% (53.76%).

In this reaction, accurate pH value tuning is critical for the synthesis of desired clusters. Compound 1 can be obtained in the pH value ranging from 4.5 to 5.0, and the best yield is attained at the pH value of about 4.7. In addition to pH value, an excessive amount of a reducing agent $N_2H_4 \cdot 2HCl$ and high temperature are also found to be important factors, which are believed to promote the reduction of Mo^{VI} to Mo^{V} and the formation of related BBs.

1.3 X-ray crystallography

Single-crystal XRD data of compound 1 were collected at 175.0 K by using a D8 VENTURE X-ray single-crystal diffractometer (Bruker, Germany) with Mo Kα radiation several times, and the best dataset was chosen to be indexed, integrated and scaled by using the APEX 3 program. The structure was solved by direct methods using the SHELXS-2014 program[45] and refined using the SHELXL-2018 program[46] through the Olex2 graphical interface[47]. All the non-hydrogen atoms except guest molecules were refined by full-matrix least-squares techniques with anisotropic displacement parameters. By using the SQUEEZE routine, a crystallographic method for eliminating scattering from disordered solvent molecules, these highly disordered solvent molecules were removed by applying a "solvent mask" embedded in Olex2 graphical interface[48]. Structures were then refined again by using the data generated. Crystallographic formulas typically contain many more water molecules in the crystal lattice than those found in the sample after drying. The structure of compound 1 was deposited at Cambridge Crystallographic Data Center, under deposition number CCDC-2348415. These data can be obtained free of charge from the Cambridge Crystallographic Data Centre via www.ccdc.cam.ac.uk/data_request/cif. The summary of the crystal data is listed in Table 1. In Table 1, a, b and c are unit cell lengths along the three crystallographic axes (x, y and z), respectively; α, β and γ are unit cell angles between the axes; ρ_{calc} is the calculated density; $F(000)$ is the total electron density at the origin of the unit cell; V is the volume of the unit cell; Z is the number of formula units per unit cell; R_{int} is the internal merging R-factor, assessing data redundancy and quality; R_1 is the conventional R-factor, evaluating agreement between the observed structure factor amplitude F_o and the calculated structure factor amplitude F_c; w_{R2} is the weighting R-factor, incorporating weighting schemes for the refinement reliability, and these R-factors measure the agreement between the crystallographic model and experimental data, where lower values indicate better fit; S_{GooF} is goodness-of-fit (GooF), indicating how well the model matches the experimental data; $\sigma(I)$ is the standard deviation of the measured reflection intensity I, representing the signal-to-noise ratio for

individual reflections.

Table 1 Crystal data and structure refinement summary for compound 1

Parameter	Value
Empirical formula	$K_{15}H_{139}Mo_{49}O_{206}$
Relative molecular mass	8 723.51
Temperature/K	175.0
Crystal system	Cubic
Space group	Pa-3
a/nm	3.142 8 (±0.001 4)
b/nm	3.142 8 (±0.001 4)
c/nm	3.142 8 (±0.001 4)
α/(°)	90
β/(°)	90
γ/(°)	90
V/nm^3	31.042 3
Z	8
ρ_{calc}/(g/cm^3)	3.324
$F(000)$	28 666.3
Reflection collected	76 906
Independent reflection	9 760 (R_{int} = 0.075 1)
S_{GooF}	1.031
Final R-factor [$I > 2\sigma(I)$]	R_1 = 0.056 9, w_{R2} = 0.146 7
R_1/w_{R2} (all data)	R_1 = 0.075 4, w_{R2} = 0.160 0

Notes: $R_1 = \sum ||F_o| - |F_c|| / \sum |F_o|$,

$w_{R2} = [\sum w(F_o^2 - F_c^2)^2 / \sum w(F_o^2)^2]^{1/2}$,

$S_{GooF} = [\sum w(F_o^2 - F_c^2)^2 / (n-p)]^{1/2}$,

where w is the weighting factor; n is the number of unique reflections; p is the number of refined parameters.

1.4 Bond valence sum (BVS) analysis

BVS analysis was performed for each bond by

$$V_{BV} = \exp[(r_0 - r)/B], \quad (1)$$

where V_{BV} represents the bond valence; r_0 is the ideal single-bond length; r is the observed bond length that measures the distance between two atoms in a crystal structure; B is the empirical constant quantifying sensitivity of the bond valence to bond length variation. BVS for each metal center is then summed from all bond valences of the bonds listed. The parameters r_0 and B were taken from Ref. [49]. The BVS for Mo^{VI} and Mo^{V} centers was calculated separately by using the corresponding parameters listed in Table 2.

Table 2 Bond valence parameters for Mo^{VI}—O and Mo^{V}—O bonds

Bond	r_0	B
Mo^{VI}—O	1.903	0.349
Mo^{V}—O	1.888	0.314

1.5 Structural analysis

The structural analysis and formula determination of the mix-valence Mo clusters have been well established in Refs. [10-11]. A combination of techniques, including BVS calculation, elemental analysis, TGA and single-crystal XRD, was employed to determine the number of reduced Mo atoms. Herein, compound 1 was selected to exemplify the general approach used to determine the formula.

The overall reduction state of compound 1 (36 electrons reduced) is confirmed by using BVS calculation. BVS calculation reveals that compound 1 is composed of a 36-electron reduced anionic skeleton containing 18 singly protonated oxygen atoms. These oxygen atoms are located at the positions of μ_3-O (μ is bridging ligand) between $\{Mo^{VI}_3\}$ and $\{Mo^{V}_2\}$ units, μ_2-O and μ_3-O on tripodal $\{Mo^{V}_6\}$ units. Moreover, all the other bridging O atoms and terminal O atoms are considered as O^{2-} based on BVS. Therefore, the oxidation states of Mo should be +5 for 36 Mo atoms and +6 for 13 Mo atoms in compound 1. Coupled with the molecular structure determined by single-crystal XRD data, the formula and overall charge could be assigned as $[Mo^{V}_{36}Mo^{VI}_{13}(OH)_{18}O_{130}]^{20-}$ (1a). To balance the negative charge of −20, 15 potassium ions and 5 protons are proposed as counterions based on elemental analysis results of K and H. The TGA curve of compound 1 exhibits an initial mass loss of 12%, which corresponds to about 58 guest water molecules. Taking into consideration the obtained information from the above calculation and data analysis, the formula of compound 1 could therefore be determined as $K_{15}H_5[Mo^{V}_{36}Mo^{VI}_{13}(OH)_{18}O_{130}] \cdot 58\ H_2O \equiv K_{15}H_5\{1a\} \cdot 58\ H_2O$. BVS values for Mo atoms in 1a are summarized in Table 3.

Table 3 BVS values for Mo atoms in 1a

Atom	BVS	Atom	BVS	Atom	BVS	Atom	BVS
Mo1	4.883	Mo6	5.189	Mo11	5.084	Mo16	5.140
Mo2	5.889	Mo7	5.106	Mo12	5.148	Mo17	6.015
Mo3	5.137	Mo8	5.203	Mo13	6.030		
Mo4	4.937	Mo9	5.048	Mo14	5.096		
Mo5	5.811	Mo10	5.054	Mo15	5.682		

1.6 Proton conductivity characterization

The fresh crystal samples were compressed into 5.0 mm diameter pellets at a pressure of 0.4 MPa, with a thickness of about 1.3 mm. Then compound 1 samples were pretreated at 98% relative humidity (RH) for 3 h. The alternating current (AC) impedance test was performed at the electrochemical workstation (CHI 760E) in a standard three-electrode system, at a frequency range of 0.1 to 1.0×10^6 Hz and an AC voltage of 50 mV, to test the proton conductivity of compound 1. As a result of the AC impedance data being equivalent to the ZSimpWin software, a Nyquist curve can be generated. The proton conductivity measurements were performed at: 1) 30 ℃ and various RHs (53%−98%); 2) 98% RH and various temperatures (30−80 ℃). The proton conductivity was calculated as

$$\sigma = \frac{L}{SR_e}, \qquad (2)$$

where σ is the proton conductivity; L is the thickness; R_e is the resistance of the pellet; S is the area of the pellet. Activation energy E_a can be calculated as

$$E_a = -k_B T(\ln \sigma_T - \ln \sigma_0), \qquad (3)$$

where σ_T is the proton conductivity at temperature T; σ_0 is the pre-exponential factor; k_B is the Boltzmann constant.

2 Results and Discussion

2.1 Structure description and analysis of compound 1

Single-crystal XRD structural analysis reveals that compound 1 crystallizes in the cubic space group Pa-3 with $a=b=c=(3.142\ 8\pm0.001\ 4)$ nm, and displays a highly reduced trigonal pyramid-like polyoxoanion structure of $[Mo^{V}_{36}Mo^{VI}_{13}(OH)_{18}O_{130}]^{20-}$. The overall structure features C_3 symmetry, and the asymmetric unit contains one-third of the formula of compound 1 (Fig. 1). From the view of BBs, the framework of 1a can be considered as an assembly of four tripodal {Mo^{V}_{6}} (Fig. 2(a)), three dumbbell-shaped {Mo^{V}_{2}} (Fig. 2(b)), one cyclic {Mo^{V}_{6}} (Fig. 2(c)), one tetrahedral {Mo^{VI}_{4}} (Fig. 2(e)) and three triangular {Mo^{VI}_{3}} (Fig. 2(f)) BBs. Hence, the overall scaffold of compound 1 displays a nanocluster with dimensions of approximately 1.4 nm × 1.8 nm, which is built by 49 Mo and 148 O atoms.

The core structure of 1a contains a trigonal pyramid-like {Mo^{V}_{36}} (Fig. 2(d)), in which the base is defined by one cyclic {Mo^{V}_{6}} BB while the main body of {Mo^{V}_{30}} is built from four tripodal {Mo^{V}_{6}} BBs and three {Mo^{V}_{2}} BBs (Fig. 2(h)). Each tripodal {Mo^{V}_{6}} BB is built from three dumbbell-shaped {Mo^{V}_{2}} units by sharing three edges and a common vertex. On the contrary, the three {Mo^{V}_{2}} units in cyclic {Mo^{V}_{6}} BB link with each other by sharing one edge. Direct connection of one cyclic {Mo^{V}_{6}} BB with one tripodal {Mo^{V}_{6}} BB can afford the archetypal MR cluster of ε-Keggin {Mo^{V}_{12}}, which is also the characteristic of C_3 symmetry. {Mo^{V}_{36}} can be regarded as an expanded version of ε-Keggin, with three {Mo^{V}_{2}} and three tripodal {Mo^{V}_{6}} BBs capping its three vertices and edges, respectively. In this kind of arrangement, {Mo^{V}_{36}} thus inherits the C_3 symmetry from ε-Keggin.

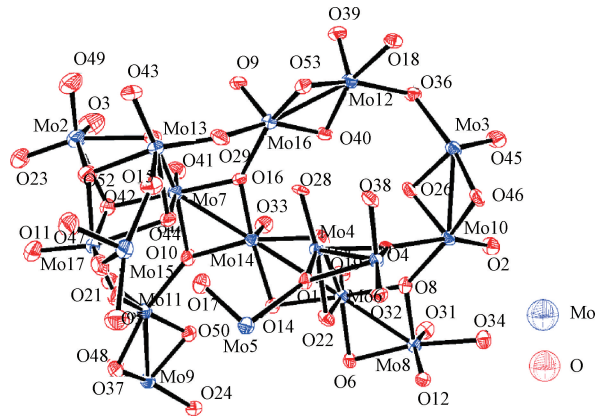

Fig. 1 Asymmetric unit of compound 1

The same core structure of {Mo^{V}_{36}} can also be found in reported {Mo_{42}}[50] where three {Mo^{VI}_{2}} BBs are located on the bottom of {Mo^{V}_{36}} and between three {Mo^{V}_{2}} and three tripodal {Mo^{V}_{6}} BBs. Instead, replacing the {Mo^{VI}_{2}} BBs with three {Mo^{VI}_{3}} BBs and placing a tetrahedral {Mo^{VI}_{4}} BB underneath the cyclic {Mo^{V}_{6}} BB affords {Mo_{49}}. In this regard, {Mo_{42}} can be proposed as an intermediate for further growth of compound 1. Moreover, the presence of three {Mo^{VI}_{3}} and one {Mo^{VI}_{4}} BBs constitutes the second base for {Mo^{V}_{36}}. The {Mo^{VI}_{3}} BB is built up by three {$Mo^{VI}O_6$} octahedrons through sharing three edges and a common μ_3-O vertex, showing a regular triangle configuration with C_3 symmetry. The Mo^{VI}—Mo^{VI} bond length is larger than 0.30 nm in this basic unit, which differs from the $Mo^{V}\cdots Mo^{V}$ separation (about 0.25 nm) in reduced {Mo^{V}_{2}} BB. The {Mo^{VI}_{3}} BB was already observed in the structure of MR cluster {Mo_{37}}[51] in which it also behaves as a capping unit to block the further growth of the central core of ε-Keggin. The tetrahedral {Mo^{VI}_{4}} BB is constructed from four corner-shared {$Mo^{VI}O_6$} octahedrons. As far as we know, such a unique BB has not been seen in reduced POM clusters, and it fits quite well with both the size and connection requirement of {Mo^{V}_{36}}, thus allowing further growth to afford compound 1. The BVS values show that the oxidation state of Mo atoms in central {Mo^{V}_{36}} is +5, while those in {Mo^{VI}_{4}} and {Mo^{VI}_{3}} units adopt a +6 oxidation state[52]. Hence the overall reduction degree of 1a reaches 73% and enters into the regime of MR clusters. The discovery of compound 1 will further stimulate the expansion of this unique family.

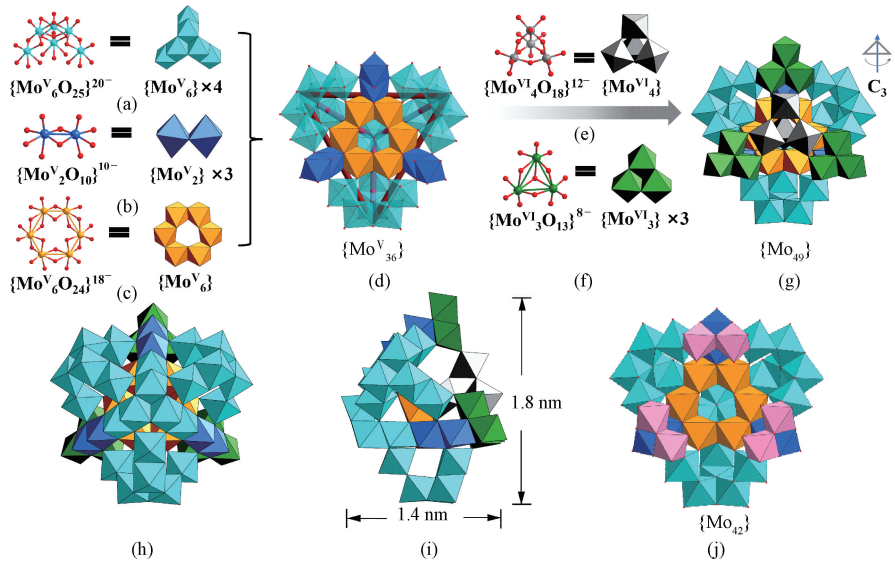

Fig. 2 Crystal structures of 1a: (a) four tripodal $\{Mo^{V}_{6}\}$; (b) three dumbbell-shaped $\{Mo^{V}_{2}\}$; (c) cyclic $\{Mo^{V}_{6}\}$; (d) $\{Mo^{V}_{36}\}$ motif; (e) tetrahedral $\{Mo^{VI}_{4}\}$; (f) three triangular $\{Mo^{VI}_{3}\}$; (g) $\{Mo_{49}\}$ cluster with C_3 symmetry; (h) back view of 1a; (i) outer dimension of 1a; (j) polyhedral view of $\{Mo_{42}\}$

To make a better comparison between compound 1 and reported $\{Mo_{42}\}$[50], the related BBs are simplified into corresponding geometrical shapes. In this context, tripodal $\{Mo^{V}_{6}\}$, cyclic $\{Mo^{V}_{6}\}$, ditopic $\{Mo^{V}_{2}\}/\{Mo^{VI}_{2}\}$, triangular $\{Mo^{VI}_{3}\}$ and tetrahedral $\{Mo^{VI}_{4}\}$ BBs are simplified as tripod, hexagon, ditopic linkers, triangle and tetrahedron, respectively (Fig. 3(b)). Consequently, the combination of all these species leads to a trigonal pyramid-like compound 1 (Fig. 3(a)). In view of the structural topology, $\{Mo_{42}\}$ displays a similar structure and symmetry to compound 1 (Fig. 3(c)). The core $\{Mo^{V}_{36}\}$ is indeed the same for both clusters, and the main difference lies in the one additional $\{Mo^{VI}_{1}\}$ cap on the brim of $\{Mo^{VI}_{2}\}$ BB as well as the tetrahedral $\{Mo^{VI}_{4}\}$ base. In this way, it can be envisioned that there is an interesting molecular growth from $\{Mo_{42}\}$ to compound 1 (Fig. 4). Such molecular growth process can also be seen for hat-like $\{Mo_{180}\}$[53], core-shell cluster $\{Mn_{40}P_{32}W_{224}\}$[54] and $\{Mo_{248}\}$[55]. We believe that exploring the molecular growth will on one hand facilitate the hierarchical assembly of complex clusters based on cluster-to-cluster growth pathway, on the other hand significantly improve understanding of the possible assembly mechanisms.

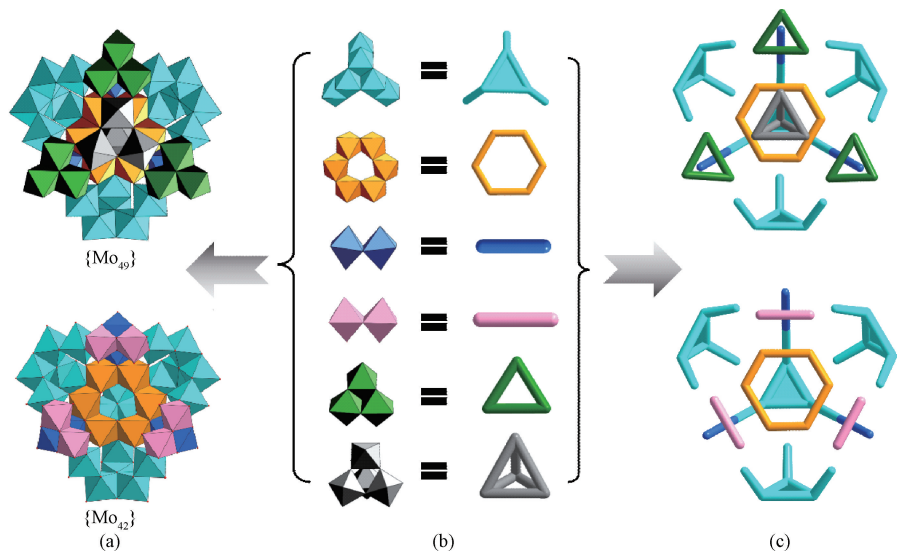

Fig. 3 Comparison between compound 1 and $\{Mo_{42}\}$: (a) polyhedral view of compound 1 and $\{Mo_{42}\}$; (b) tripodal $\{Mo^{V}_{6}\}$, cyclic $\{Mo^{V}_{6}\}$, ditopic $\{Mo^{V}_{2}\}/\{Mo^{VI}_{2}\}$, triangular $\{Mo^{VI}_{3}\}$ and tetrahedral $\{Mo^{VI}_{4}\}$ BBs simplified as tripod, hexagon, ditopic linkers, triangle and tetrahedron; (c) simplified metallic skeleton of compound 1 and $\{Mo_{42}\}$

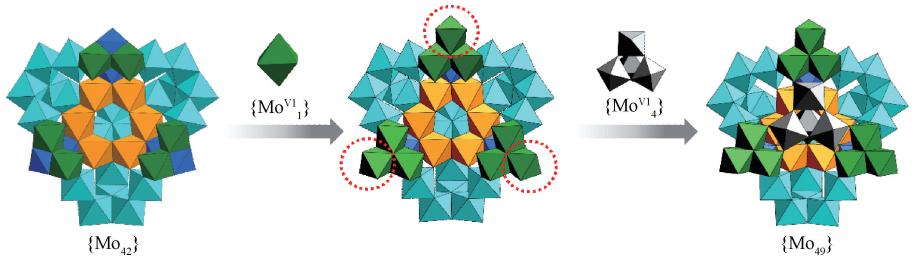

Fig. 4 Molecular growth from {Mo_{42}} to compound 1

Although the nuclearity of compound 1 is not as high as {Mo_{60}}, {$Mo_{60}Ni_8Ln_6$} and {Mo_{240}}, it should be noted that compound 1 consists of five types of BBs, rendering it as one of the MR clusters bearing the largest variety of BBs. Another example can be found in {$Mo_{70}Ln_5$} which is also constructed from five types of BBs and shows a unique star-like structure. This means that the structure of compound 1 is indeed complex. If more BBs can be discovered and the connection modes between different BBs can be tuned in a controlled way, then complex and diverse MR clusters will be developed more efficiently based on this BB strategy.

2.2 Spectroscopic characterization of compound 1

The FTIR spectrum of compound 1 exhibits strong peaks at 956 cm^{-1} and 729 cm^{-1}, assigned to the stretching vibrations of the terminal Mo═O and Mo—O bonds, respectively. The peak at 571 cm^{-1} corresponds to the vibrations of Mo—O—Mo bridges (Fig. 5(a)). Analysis of the Raman spectrum of compound 1 shows a similar result to FTIR, where the strong bands centered around 990 cm^{-1} and 813 cm^{-1} are characteristics of the vibrations for terminal Mo═O bonds and Mo—O—Mo bridges (Fig. 5(b))[16, 23]. TGA reveals that the initial mass loss of 12% corresponds to the elimination of about 58 free water molecules (Fig. 5(c)). Afterward, the framework of compound 1 starts to collapse and finally transforms into the related metal oxides. The good agreement between experimental and simulated XRD patterns confirms the phase purity of compound 1 (Fig. 5(d)).

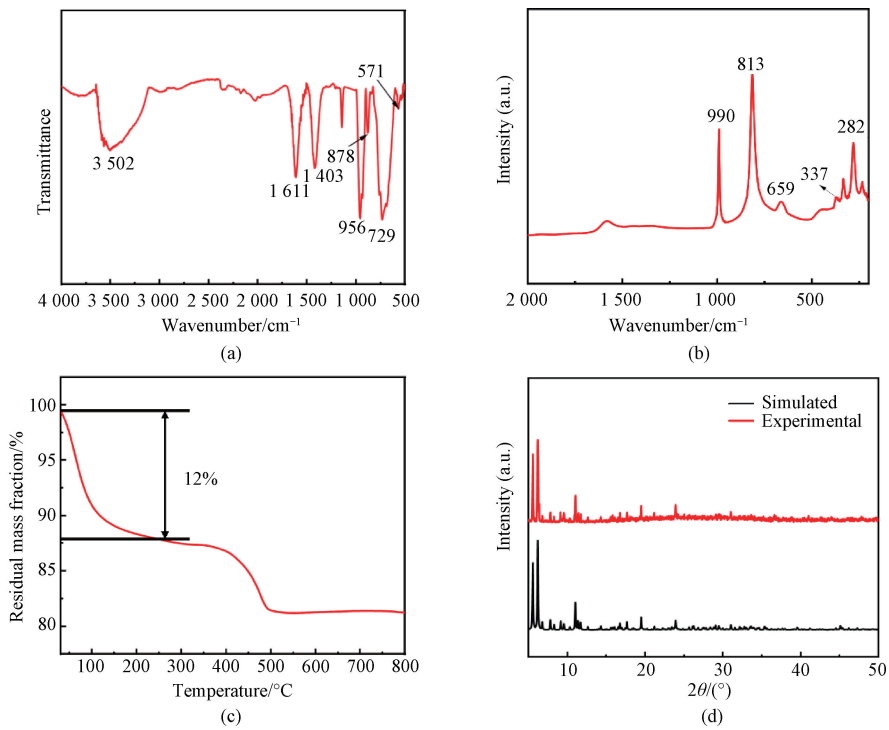

Fig. 5 Characterization of compound 1: (a) FTIR spectrum; (b) Raman spectrum; (c) TGA curve; (d) XRD patterns

2.3 Proton conductivity

Due to their fast mobility rate and high proton capacity, POMs have become widely used materials in proton conduction[56-59]. Compound 1 exhibits potential as a solid-state proton conductor due to its abundant proton counterions and oxygen-rich surface. To evaluate its proton conductivity σ, we employed AC impedance spectroscopy on compacted pellet samples of compound 1 at various RHs and temperatures.

Firstly, the effect of RH on the proton conductivity

was studied for compound 1 at 30 ℃. In Nyquist curves shown in Figs. 6(a) and 6(c), Z' represents the real part of complex impedance, corresponding to resistive components; Z'' denotes the imaginary part, reflecting reactive components associated with capacitive behaviors. When switching RH from 53% to 98%, the proton conductivity of compound 1 is continuously enhanced from 2.51×10^{-6} to 2.88×10^{-3} S/cm (Figs. 6(a) and 6(b)), which might be caused by more proton transfer sites from water molecules. Then, the temperature-dependent proton conductivity was tested in a temperature range of 30 to 80 ℃ at RH of 98%. The proton conductivity raises dramatically from 2.88×10^{-3} to 7.88×10^{-3} S/cm (Fig. 6(c)). This could be ascribed to the generation of more hydronium ions from water molecules and protons at elevated temperatures[55]. In addition, the proton conductivity of compound 1 is comparable to that of several archetypal POMs such as $\{Mo_{132}\}$[23], $\{Bi_{18}Ce_{12}W_{74}\}$[60], $\{P_2W_{18}\} \subset \{Mo_{24}Fe_{12}\}$[61], $(1H\text{-}1,2,4\text{-triazole})_8\{V_{10}\}$[62], $\{Dy_{10}Nb_{190}\}$[63] and $\{Nb_{68}O_{200}\}$[64], indicating its potential as solid-state proton conductor. According to the Arrhenius equation, the activation energy E_a for proton transfer in compound 1 at 98% RH is 0.17 eV (Fig. 6(d)). This low E_a value (between 0.10 eV and 0.40 eV) suggests that the Grotthuss mechanism is the dominant pathway for proton conduction[65]. The high proton conductivity can be primarily attributed to the extensive hydrogen bond network. This network is formed by the abundant coordination of water molecules and rich surface oxygen atoms of $\{Mo_{49}\}$, and can provide multiple channels for proton movement and facilitate the formation of a continuous network for efficient proton hopping. Figure 7 shows the proposed proton conduction pathway of compound 1, and the gray ball represents the proton.

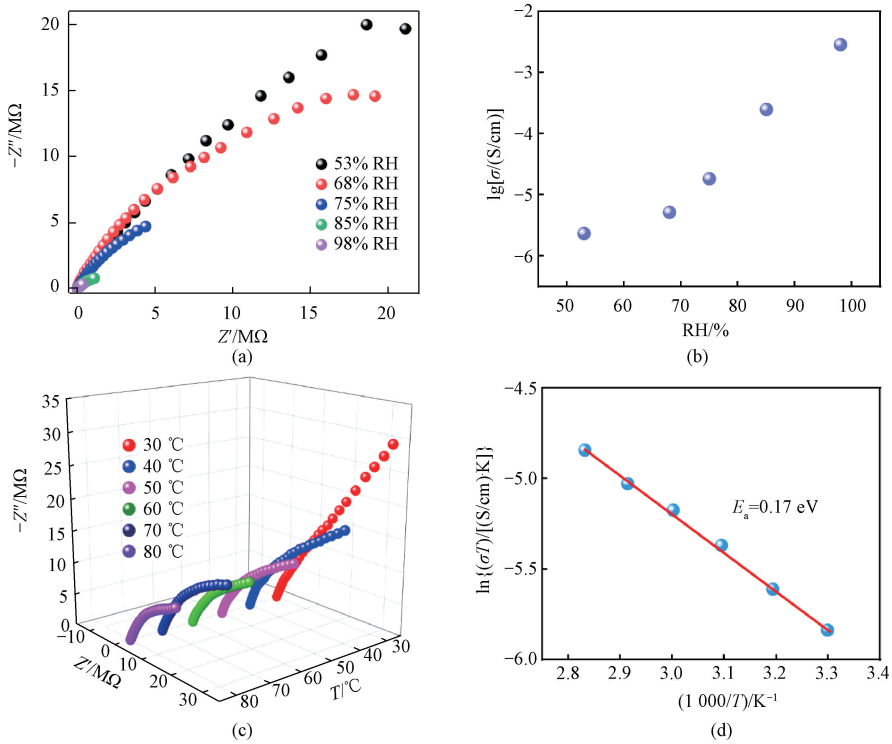

Fig. 6 Proton conductivity of compound 1 at various RHs and temperatures: (a) Nyquist curves at 30 ℃ and various RHs; (b) humidity-dependent proton conductivity at 30 ℃; (c) Nyquist curves at various temperatures and 98% RH; (d) Arrhenius plot at various temperatures and 98% RH

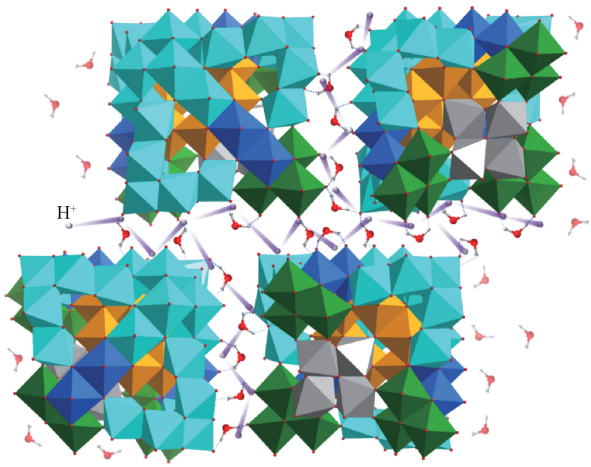

Fig. 7 Proposed proton conduction pathway of compound 1

The stability of compound 1 was confirmed by the heating and cooling cycle (30 – 80 ℃) at 98% RH (Fig. 8(a)). The cooling and heating conductivity curves are nearly the same, suggesting good stability and conductivity durability. In addition, the XRD patterns and FTIR spectra of compound 1 after proton conduction are in good agreement with pristine samples, showing that the structure of compound 1 remains stable during the measurement (Figs. 8(b) and 8(c)). Overall, the good performance of compound 1 in proton conduction manifests the great potential of using highly reduced POM clusters as proton conductors in energy-based applications.

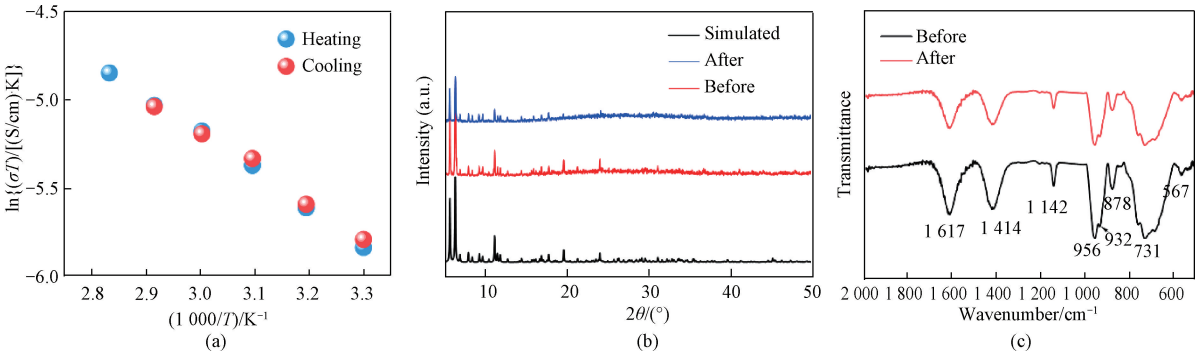

Fig. 8 Stability of compound 1 before and after proton conduction: (a) Arrhenius plots of proton conductivity during one heating and cooling cycle at 98% RH; (b) XRD patterns; (c) FTIR spectra

3 Conclusions

In conclusion, a novel highly reduced POM cluster {Mo_{49}} featuring a trigonal pyramid-like structure was synthesized and applied for proton conduction. With the guided assembly of the tetrahedral {Mo^{VI}_4} BB, the core structure {Mo_{36}} constructed from classical {Mo^{V}_6} and {Mo^{V}_2} facilely evolves to {Mo_{49}}. Moreover, the molecular structure of {Mo_{49}} can be considered as an expanded version of {Mo_{42}}, with three additional {Mo^{VI}} units capping on the brim of {Mo_{42}} and the tetrahedral {Mo^{VI}_4} as base. Proton conductivity measurement indicates that compound 1 presents an optimal conductivity of 7.88×10^{-3} S/cm at 80 ℃ and 98% RH owing to the facile hydrogen-bonding network for proton transfer. This work may promote the rational and controllable assembly of POM materials with novel properties by using the BB strategy.

References

[1] LONG D L, TSUNASHIMA R, CRONIN L. Polyoxometalates: building blocks for functional nanoscale systems [J]. *Angewandte Chemie International Edition*, 2010, 49(10): 1736-1758.

[2] LIU Y F, HU Q L, CHEN X J, et al. Two sandwich-type uranyl-containing polytungstates catalyze aerobic synthesis of benzimidazoles[J]. *Rare Metals*, 2024, 43(3): 1316-1322.

[3] LIU Y F, ZENG G D, CHENG Y T, et al. A $H_4SiW_{12}O_{40}$-catalyzed three-component tandem reaction for the synthesis of 3, 3-disubstituted isoindolinones [J]. *Chinese Chemical Letters*, 2024, 35(1): 108480.

[4] DING J H, LIU Y F, TIAN Z T, et al. Uranyl-silicotungstate-containing hybrid building units {α-SiW_9} and {γ-SiW_{10}} with excellent catalytic activities in the three-component synthesis of dihydropyrimidin-2(1H)-ones [J]. *Inorganic Chemistry Frontiers*, 2023, 10(11): 3195-3201.

[5] LI K, LIU Y F, LIN X L, et al. Copper-containing polyoxometalate-based metal-organic frameworks as heterogeneous catalysts for the synthesis of *N*-heterocycles [J]. *Inorganic Chemistry*, 2022, 61(18): 6934-6942.

[6] GUMEROVA N I, ROMPEL A. Synthesis, structures and applications of electron-rich

polyoxometalates [J]. *Nature Reviews Chemistry*, 2018, 2: 112.
[7] MONAKHOV K Y, BENSCH W, KÖGERLER P. Semimetal-functionalised polyoxovanadates [J]. *Chemical Society Reviews*, 2015, 44(23): 8443-8483.
[8] WANG S S, YANG G Y. Recent advances in polyoxometalate-catalyzed reactions [J]. *Chemical Reviews*, 2015, 115(11): 4893-4962.
[9] NISHIMOTO Y, YOKOGAWA D, YOSHIKAWA H, et al. Super-reduced polyoxometalates: excellent molecular cluster battery components and semipermeable molecular capacitors[J]. *Journal of the American Chemical Society*, 2014, 136(25): 9042-9052.
[10] XUAN W M, POW R, ZHENG Q, et al. Ligand-directed template assembly for the construction of gigantic molybdenum blue wheels [J]. *Angewandte Chemie International Edition*, 2019, 58(32): 10867-10872.
[11] RIBÓ E G, BELL N L, XUAN W M, et al. Synthesis, assembly, and sizing of neutral, lanthanide substituted molybdenum blue wheels $\{Mo_{90}Ln_{10}\}$ [J]. *Journal of the American Chemical Society*, 2020, 142(41): 17508-17514.
[12] LI J, ZHANG D, CHI Y N, et al. Catalytic application of polyoxovanadates in the selective oxidation of organic molecules [J]. *Polyoxometalates*, 2022, 1(2): 9140012.
[13] LIU J, JIANG N, LIN J M, et al. Structural evolution of giant polyoxometalate: from "keplerate" to "lantern" type Mo_{132} for improved oxidation catalysis [J]. *Angewandte Chemie International Edition*, 2023, 62(33): e202304728.
[14] REZAEIFARD A, HADDAD R, JAFARPOUR M, et al. $\{Mo_{132}\}$ nanoball as an efficient and cost-effective catalyst for sustainable oxidation of sulfides and olefins with hydrogen peroxide[J]. *ACS Sustainable Chemistry & Engineering*, 2014, 2(4): 942-950.
[15] LI X X, JI T, GAO J Y, et al. An unprecedented fully reduced $\{Mo^{V}_{60}\}$ polyoxometalate: from an all-inorganic molecular light-absorber model to improved photoelectronic performance[J]. *Chemical Science*, 2022, 13(16): 4573-4580.
[16] RIBÓ E G, BELL N L, LONG D L, et al. Engineering highly reduced molybdenum polyoxometalates via the incorporation of *d* and *f* block metal ions [J]. *Angewandte Chemie International Edition*, 2022, 61(21): e202201672.
[17] ZHOU D X, LI B B, ZHAO Q X, et al. Solvent-modulated assembly of peptide and cerium functionalized gigantic $\{Mo_{120}Ce_6\}_2$ dimers for high-efficiency photocatalytic oxidation [J]. *Inorganic Chemistry Frontiers*, 2024, 11(8): 2355-2364.
[18] ZANG D J, WANG H Q. Polyoxometalate-based nanostructures for electrocatalytic and photocatalytic CO_2 reduction [J]. *Polyoxometalates*, 2022, 1(1): 9140006.
[19] LIU Y F, LIN X L, MING B M, et al. Three polyoxometalate-based Ag-organic compounds as heterogeneous catalysts for the synthesis of benzimidazoles[J]. *Inorganic Chemistry*, 2024, 63(12): 5681-5688.
[20] YANG Y, ZHAO Q X, XUAN W M, et al. Photoactive naphthalene diimide functionalized titanium-oxo clusters with high photoelectrochemical responses [J]. *Journal of Donghua University (English Edition)*, 2023, 40(6): 590-599.
[21] LIAO L R, ZHENG D C, OU P X, et al. π-conjugated chromophore functionalized high-nuclearity titanium-oxo clusters containing structural unit of anatase for photocatalytic selective oxidation of sulfides[J]. *Rare Metals*, 2024, 43(4): 1736-1746.
[22] WANG H Y, LI S R, WANG X, et al. Enhanced proton conductivity of Mo_{154}-based porous inorganic framework[J]. *Science China Chemistry*, 2021, 64(6): 959-963.
[23] LI X X, LI C H, HOU M J, et al. Ce-mediated molecular tailoring on gigantic polyoxometalate $\{Mo_{132}\}$ into half-closed $\{Ce_{11}Mo_{96}\}$ for high proton conduction[J]. *Nature Communications*, 2023, 14(1): 5025.
[24] LIU W J, DONG L Z, LI R H, et al. Different protonic species affecting proton conductivity in hollow spherelike polyoxometalates [J]. *ACS Applied Materials & Interfaces*, 2019, 11(7): 7030-7036.
[25] JI F, JIANG F Y, LUO H W, et al. Hybrid membrane of sulfonated poly(aryl ether ketone sulfone) modified by molybdenum clusters with enhanced proton conductivity[J]. *Small*, 2024, 20(33): 2312209.
[26] ZHANG H, YU K, LI J S, et al. The highest connected pure inorganic 3D framework assembled by $\{P_4Mo_6\}$ cluster and alkali metal potassium[J]. *RSC Advances*, 2015, 5(5): 3552-3559.
[27] YIN X Y, BI H X, SONG H, et al. Photoactive hourglass-type $M\{P_4Mo_6\}_2$ networks for efficient removal of hexavalent chromium [J]. *Polyoxometalates*, 2023, 2(2): 9140027.
[28] GAO Z X, SUN S, LI B, et al. Design and synthesis of phosphomolybdate coordination compounds based on $\{P_4Mo_6\}$ structural units and their proton conductivity [J]. *Tungsten*,

2023, 5(1): 67-74.
[29] LIN J M, LI N, YANG S P, et al. Self-assembly of giant Mo_{240} hollow opening dodecahedra[J]. *Journal of the American Chemical Society*, 2020, 142(32): 13982-13988.
[30] MÜLLER A, BECKMANN E, BÖGGE H, et al. Inorganic chemistry goes protein size: a Mo_{368} nano-hedgehog initiating nanochemistry by symmetry breaking [J]. *Angewandte Chemie International Edition*, 2002, 41(7): 1162-1167.
[31] MÜLLER A, KRICKEMEYER E, BÖGGE H, et al. Formation of a ring-shaped reduced "metal oxide" with the simple composition $[(MoO_3)_{176}(H_2O)_{80}H_{32}$ [J]. *Angewandte Chemie International Edition*, 1998, 37(9): 1220-1223.
[32] MÜLLER A, KRICKEMEYER E, MEYER J, et al. $Mo_{154}(NO)_{14}O_{420}(OH)_{28}(H_2O)_{70}]^{(25\pm5)-}$: a water-soluble big wheel with more than 700 atoms and a relative molecular mass of about 24 000 [J]. *Angewandte Chemie International Edition in English*, 1995, 34(19): 2122-2124.
[33] MÜLLER A, KRICKEMEYER E, BÖGGE H, et al. Organizational forms of matter: an inorganic super fullerene and keplerate based on molybdenum oxide [J]. *Angewandte Chemie International Edition*, 1998, 37(24): 3359-3363.
[34] WANG Y R, HUANG Q, HE C T, et al. Oriented electron transmission in polyoxometalate-metalloporphyrin organic framework for highly selective electroreduction of CO_2 [J]. *Nature Communications*, 2018, 9(1): 4466.
[35] BARMAN S, SREEJITH S S, GARAI S, et al. Selective photocatalytic carbon dioxide reduction by a reduced molybdenum-based polyoxometalate catalyst[J]. *ChemPhotoChem*, 2019, 3(2): 93-100.
[36] SONG Y F. Polyoxometalate-based assemblies and functional materials[M]. Cham: Springer International Publishing, 2018.
[37] POPE M T, MÜLLER A. Polyoxometalate chemistry from topology via self-assembly to applications[M]. Cham: Springer Netherlands, 2001.
[38] LAI Q S, LI X X, ZHENG S T. All-inorganic POM cages and their assembly: a review[J]. *Coordination Chemistry Reviews*, 2023, 482: 215077.
[39] JIANG H, ZHANG W Q, HOU B, et al. Planar chiral [2.2] paracyclophane-based Zr(IV) metal-organic frameworks[J]. *CCS Chemistry*, 2023, 5(7): 1635-1643.
[40] LIU J C, ZHAO J W, STREB C, et al. Recent advances on high-nuclear polyoxometalate clusters [J]. *Coordination Chemistry Reviews*, 2022, 471: 214734.
[41] COLLIARD I, BROWN J C, FAST D B, et al. Snapshots of Ce_{70} toroid assembly from solids and solution[J]. *Journal of the American Chemical Society*, 2021, 143(25): 9612-9621.
[42] ZHU Z K, ZHANG J, CONG Y C, et al. Two giant calixarene-like polyoxoniobate nanocups {$Cu_{12}Nb_{120}$} and {$Cd_{16}Nb_{128}$} built from mixed macrocyclic cluster motifs [J]. *Angewandte Chemie International Edition*, 2022, 61(7): e202113381.
[43] ZHANG H L, LI A, LI K, et al. Ultrafiltration separation of Am(VI)-polyoxometalate from lanthanides [J]. *Nature*, 2023, 616(7957): 482-487.
[44] LI B B, LAN Y X, SU H Y, et al. {Mo_4}-directed structural evolution of highly reduced molybdenum red clusters for efficient proton conduction[J]. *Dalton Transactions*, 2024, 53(14): 6184-6189.
[45] SHELDRICK G M. Crystal structure refinement with SHELXL [J]. *Acta Crystallographica Section C: Structural Chemistry*, 2015, 71(part 1): 3-8.
[46] SHELDRICK G M. SHELXT-integrated space-group and crystal-structure determination [J]. *Acta Crystallographica Section A: Fundation and Advances*, 2015, 71(part 1): 3-8.
[47] DOLOMANOV O V, BOURHIS L J, GILDEA R J, et al. OLEX2: a complete structure solution, refinement and analysis program[J]. *Journal of Applied Crystallography*, 2009, 42(2): 339-341.
[48] REES B, JENNER L, YUSUPOV M. Bulk-solvent correction in large macromolecular structures[J]. *Acta Crystallographica Section D: Structural Biology*, 2005, 61(9): 1299-1301.
[49] GAGNÉ O C, HAWTHORNE F C. Comprehensive derivation of bond-valence parameters for ion pairs involving oxygen[J]. *Acta Crystallographica Section B: Structural Science, Crystal Engineering and Materials*, 2015, 71(5): 562-578.
[50] KHAN M I, CHEN Q, SALTA J, et al. Retention of structural cores in the synthesis of high-nuclearity polyoxoalkoxomolybdate clusters encapsulating $[Na(H_2O)_3]^+$ and $[MoO_3]$ moieties. Hydrothermal syntheses and structures of $(NH_4)_7[NaH_{12}Mo_{16}O_{52}]\cdot 4H_2O$ and $(Me_3NH)_4K_2[H_{14}Mo_{16}O_{52}]\cdot 8H_2O$ and their structural relationships to the class of superclusters $[XH_nMo_{42}O_{109}\{(OCH_2)_3CR\}_7]^{m-}$ (X = $Na(H_2O)_3^+$: $n=13$, $m=9$; $n=15$, $m=7$. X = MoO_3: $n=14$, $m=9$; $n=13$, $m=10$) [J]. *Inorganic Chemistry*, 1996, 35(7): 1880-1901.
[51] YAMASE T, ISHIKAWA E. Photochemical self-assembly reaction of β-$[Mo_8O_{26}]^{4-}$ to mixed-

valence cluster $[Mo_{37}O_{112}]^{26-}$ in aqueous media [J]. *Langmuir*, 2000, 16(23): 9023-9030.

[52] ATOVMYAN L O, KRASOCHKA O N. X-ray diffraction investigation of the crystals of the octamolybdate $(NH4)_4Mo_8O_{26} \cdot 4H_2O$ [J]. *Journal of Structural Chemistry*, 1972, 13(2): 319-320.

[53] XUAN W M, POW R, LONG D L, et al. Exploring the molecular growth of two gigantic half-closed polyoxometalate clusters $\{Mo_{180}\}$ and $\{Mo_{130}Ce_6\}$ [J]. *Angewandte Chemie International Edition*, 2017, 56(33): 9727-9731.

[54] FANG X K, KÖGERLER P, FURUKAWA Y, et al. Molecular growth of a core-shell polyoxometalate [J]. *Angewandte Chemie International Edition*, 2011, 50(22): 5212-5216.

[55] MÜLLER A, SHAH S Q N, BÖGGE H, et al. Molecular growth from a Mo_{176} to a Mo_{248} cluster [J]. *Nature*, 1999, 397: 48-50.

[56] OGIWARA N, IWANO T, ITO T, et al. Proton conduction in ionic crystals based on polyoxometalates [J]. *Coordination Chemistry Reviews*, 2022, 462: 214524.

[57] MENG X, WANG H N, SONG S Y, et al. Proton-conducting crystalline porous materials [J]. *Chemical Society Reviews*, 2017, 46(2): 464-480.

[58] SAHOO R, PAL S C, DAS M C. Solid-state proton conduction driven by coordinated water molecules in metal-organic frameworks and coordination polymers[J]. *ACS Energy Letters*, 2022, 7(12): 4490-4500.

[59] CHAND S, ELAHI S M, PAL A, et al. Metal-organic frameworks and other crystalline materials for ultrahigh superprotonic conductivities of 10^{-2} S cm^{-1} or higher [J]. *Chemistry—A European Journal*, 2019, 25(25): 6259-6269.

[60] LIU J C, HAN Q, CHEN L J, et al. Aggregation of giant cerium-bismuth tungstate clusters into a 3D porous framework with high proton conductivity [J]. *Angewandte Chemie International Edition*, 2018, 130(28): 8552-8556.

[61] ZHU M H, IWANO T, TAN M J, et al. Macrocyclic polyoxometalates: selective polyanion binding and ultrahigh proton conduction [J]. *Angewandte Chemie International Edition*, 2022, 61(15): e202200666.

[62] CAO J P, SHEN F C, LUO X M, et al. Proton conductivity resulting from different triazole-based ligands in two new bifunctional decavanadates [J]. *RSC Advances*, 2018, 8(33): 18560-18566.

[63] LAI R D, ZHANG J, LI X X, et al. Assemblies of increasingly large Ln-containing polyoxoniobates and intermolecular aggregation-disaggregation interconversions [J]. *Journal of the American Chemical Society*, 2022, 144(42): 19603-19610.

[64] LIN Y D, ZHU Z K, GE R, et al. Proton conductive polyoxoniobate frameworks constructed from nanoscale $\{Nb_{68}O_{200}\}$ cages [J]. *Chemical Communications*, 2021, 57(38): 4702-4705.

[65] KIM S, JOARDER B, HURD J A, et al. Achieving superprotonic conduction in metal-organic frameworks through iterative design advances[J]. *Journal of the American Chemical Society*, 2018, 140(3): 1077-1082.

基于构筑块导向组装策略设计合成钼红簇合物{Mo_{49}}及其质子传导性能研究

张对对[1]，陈泽宇[1]，唐荣庆[1]，龚腾飞[2]，邵志宇[1*]，宣为民[1*]

1. 东华大学 先进纤维材料全国重点实验室，化学与化工学院，上海 201620

2. 嘉兴市嘉源检测技术服务有限公司，浙江 嘉兴 314000

摘　要：具有高还原态的钼红簇合物作为一种新兴的多钼氧酸盐簇合物，在能量转换、存储和催化等方面表现出作为电子或质子存储库的巨大潜力。然而，其有限的结构种类极大地阻碍了对这类簇合物作为功能材料发展的进一步探索。该文描述了一种基于多种基本构筑块的合理组装所形成的新型高度还原的钼红簇合物 {Mo_{49}}（化合物 1）。除了存在钼红簇合物家族中已报道的基本构筑块外，独特的四面体型 {Mo^{VI}_4} 构筑块对三角锥构型的化合物 1 的组装具有非常重要的指导作用。该化合物的多钼氧酸盐骨架部分由 49 个钼原子和 148 个氧原子组成，还原度高达 73%。此外，在 80 ℃和相对湿度为 98%的条件下，化合物 1 压片样品的质子传导率为 7.88×10^{-3} S/cm，这是因为表面氧原子、质子和客体水分子之间形成了有效的氢键网络。该研究为通过构筑块策略组装和合成钼红簇合物提供了新见解，并展示了其在先进应用领域的巨大潜力。

关键词：多钼氧酸盐；高还原态簇合物；构筑块；质子传导率